

COMPARISON BETWEEN Mg II *k* AND Ca II H IMAGES RECORDED BY SUNRISE/SuFI

S. DANILOVIC¹, J. HIRZBERGER¹, T. L. RIETHMÜLLER¹, S. K. SOLANKI^{1,2}, P. BARTHOL¹, T. BERKEFELD³, A. GANDORFER¹,
L. GIZON^{1,4}, M. KNÖLKER⁵, W. SCHMIDT³, J. BLANCO RODRÍGUEZ⁶, AND J. C. DEL TORO INIESTA⁷

¹ Max-Planck-Institut für Sonnensystemforschung, Max-Planck-Str. 2, D-37191 Katlenburg-Lindau, Germany; danilovic@mps.mpg.de

² School of Space Research, Kyung Hee University, Yongin, Gyeonggi, 446-701, Korea

³ Kiepenheuer-Institut für Sonnenphysik, Schöneckstr. 6, D-79104 Freiburg, Germany

⁴ Institut für Astrophysik Georg-August-Universität Göttingen, Friedrich-Hund-Platz 1, D-37077 Göttingen, Germany

⁵ High Altitude Observatory, National Center for Atmospheric Research, P.O. Box 3000, Boulder, CO 80307-3000, USA

⁶ Image Processing Laboratory, University of Valencia, P.O. Box 22085, E-46980 Paterna, Valencia, Spain

⁷ Instituto de Astrofísica de Andalucía (CSIC), Apartado de Correos 3004, E-18080 Granada, Spain

Received 2013 November 6; accepted 2014 January 26; published 2014 February 27

ABSTRACT

We present a comparison of high-resolution images of the solar surface taken in the Mg II *k* and Ca II H channels of the Filter Imager on the balloon-borne solar observatory SUNRISE. The Mg and Ca lines are sampled with 0.48 nm and 0.11 nm wide filters, respectively. The two channels show remarkable qualitative and quantitative similarities in the quiet Sun, in an active region plage and during a small flare. However, the Mg filtergrams display 1.4–1.7 times higher intensity contrast and appear more smeared and smoothed in the quiet Sun. In addition, the fibrils in a plage are wider. Although the exposure time is 100 times longer for Mg images, the evidence suggests that these differences cannot be explained only with instrumental effects or the evolution of the solar scene. The differences at least partially arise because of different line-formation heights, the stronger response of Mg *k* emission peaks to the higher temperatures, and the larger height range sampled by the broad Mg filter used here. This is evidently manifested during the flare when a surge in Mg evolves differently than in Ca.

Key words: Sun: activity – Sun: chromosphere – techniques: photometric

Online-only material: color figures

1. INTRODUCTION

Studies of the chromosphere suffer from multiple problems. This layer of the atmosphere is particularly hard to model because of the near-equipartition in energy between magnetic field, the thermal energy of the gas, and its kinetic energy. Complex physical processes that are often neglected need to be taken into account, such as three-dimensional non-local thermodynamic equilibrium (NLTE) radiative transfer, time-dependent ionization, and ambipolar diffusion. From an observational point of view, a hinderance is the relative lack of chromospheric diagnostics available without needing to go to space. Besides the well-studied spectral lines accessible from the ground, such as H α , Ca II H, and K, the Ca II infrared triplet, and the He I triplet at 10830 Å, the Mg II *h* and *k* lines can be observed from a balloon and from space. Since they couple strongly with temperature up to relatively high in the chromosphere (Milkey & Mihalas 1974; Uitenbroek 1997; Leenaarts et al. 2013a, 2013b), these lines have the potential to provide information on chromospheric structure and dynamics that is complementary (at least in some respects) to that obtained from the other spectral lines.

So far, only relatively few observations of the Mg II *h* and *k* lines have been reported. The first Mg II *h* and *k* spectra in an active region and at different heliocentric angles were obtained with rocket-borne spectrometers (Allen & McAllister 1978; Kohl & Parkinson 1976). The Ultraviolet Spectrometer and Polarimeter on board the *Solar Maximum Mission* (Woodgate et al. 1980) provided the first space-based high-resolution spectra, while the first simultaneous observations with Lyman α and β , and the Ca II H and K lines were carried out with the Laboratoire de Physique Stellaire et Planétaire (LPSP) instrument on board the *Orbiting Solar Observatory (OSO) 8*

(Bonnet et al. 1978). The French balloon experiment RASOLBA (Staath & Lemaire 1995) and later the sounding-rocket experiments high-resolution telescope spectrometer-9 (HRTS; Morrill et al. 2001; Morrill & Korendyke 2008) acquired first high spatial resolution Mg II *h* and *k* spectra, as also did the Solar Ultraviolet Magnetograph Investigation (West et al. 2007, 2011). Since 2013 September, spectra and imaging in the Mg II *h* and *k* line are collected regularly with the Interface Region Imaging Spectrograph (De Pontieu et al. 2014), at a spatial resolution of 0".3. Before that, in 2013 June, the balloon-borne observatory, SUNRISE (Solanki et al. 2010; Barthol et al. 2011), had its second science flight, which provided the Mg II *k* images with the highest spatial resolution so far. The first results were presented in Riethmüller et al. (2013).

In this paper, we extend their work and present a comparison of high-resolution images taken in the Mg II *k* and Ca II H channels of the SUNRISE Filter Imager (SuFI; Gandorfer et al. 2011) during the same SUNRISE flight.

2. OBSERVATIONAL DATA

The second science flight of SUNRISE took place in the period 2013 June 12–17. The balloon flew from Kiruna in Sweden to Boothia in Canada at an altitude of roughly 37 km. A total of 105 images were recorded in Mg II *k* with a 0.48 nm wide filter, often together with data at other wavelengths. Here, we compare with observations in the narrow 0.11 nm broad Ca II H filter and partly with the roughly 5 nm broad 300 nm filter. Integration times were 50 s for the Mg II *k* channel, 500 ms for Ca II H, and 50 ms for 300 nm. The data were reduced as described by Riethmüller et al. (2013). In particular, they were phase-diversity reconstructed to produce level 2 data (Hirzberger et al. 2010, 2011). Furthermore, we concentrate on

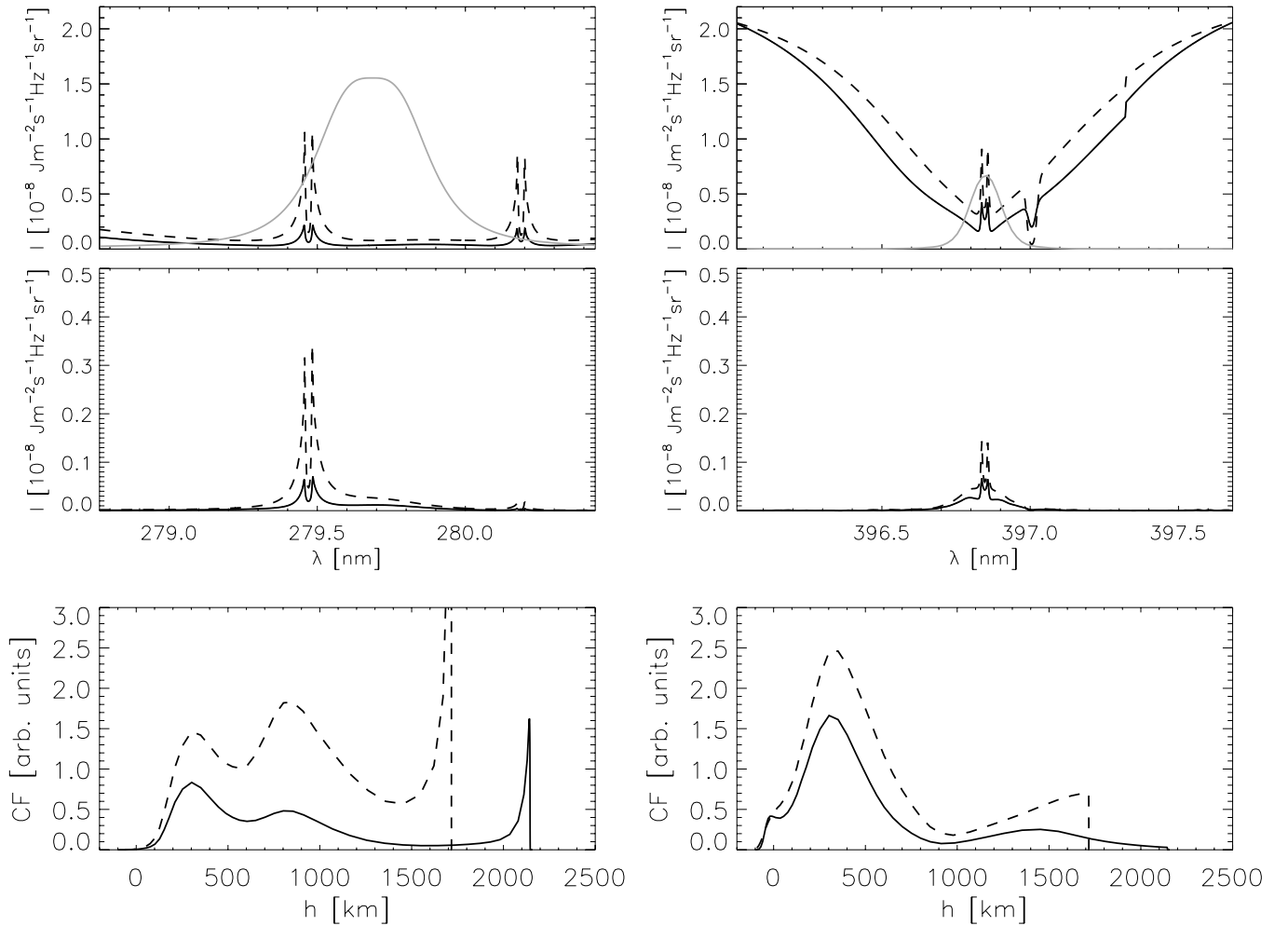


Figure 1. Synthesized Mg II *h* and *k* (left column) and Ca II H (right column) profiles calculated in FAL-C (solid) and FAL-P (dashed) with the corresponding SuFI filter profiles in gray (first row), the same intensity profiles multiplied with the transmission curves (second row) and the corresponding contribution functions integrated over the whole transmitted wavelength range (third row).

the two SuFI channels most likely to contain chromospheric signatures: the Mg II *k* and the narrow (i.e., 0.11 nm wide) Ca II H channel (for brevity, hereafter simply called Mg and Ca channels, respectively). All images are resampled by averaging spatially 3×3 pixels in order to increase the signal-to-noise ratio (S/N).

3. CONTRIBUTION FUNCTIONS AND COUPLING TO LOCAL TEMPERATURE

The finite width of the SuFI filters (which are close to the narrowest values that can currently be achieved by interference filters at these wavelengths) imply that the images recorded by SuFI get significant contributions from the line wings (see Figure 1 of Riethmüller et al. 2013 for the Mg channel). This also means that these channels get a significant contribution from the photosphere. To determine which heights the SuFI images sample, we computed contribution functions (CFs) of Mg II *k* and Ca II H in partial redistribution using the RH code (Uitenbroek 2001) and the one-dimensional semi-empirical model atmospheres FAL-C and FAL-P (Fontenla et al. 1999). We use the four-level plus continuum Ca II model atom (Uitenbroek 2001) and the 10 level plus continuum Mg II atom (Uitenbroek 1997). Besides hydrogen, which is also treated in NLTE, no blends are included.

The computed line profiles are displayed in the top panels of Figure 1 together with the SuFI filter profiles (in the case of Mg II, both *h* and *k* lines were computed because of the width of the SuFI filter). In the second row, the computed profiles are plotted after multiplication with the filter profile. For both lines, the core provides a large contribution to the radiation sampled by the filter. In the quiet Sun, the relative contribution of the wings to the light transmitted through the filter is roughly similar for both lines (solid curves). In plage, however, the Mg II *h* core is enhanced more and hence provides a larger contribution to its respective SuFI channel than the core of Ca II H. The contribution of H ϵ , located not far from the core of Ca II H, is negligible because of the width of the Ca filter. That is when observed on disk. Off limb, though, this may not be true. Beck et al. (2013) estimated that up to about one-third of the off-limb intensity comes from H ϵ emission when using a filter with a width of 0.3 nm centered at the Ca II H line core.

The CFs, obtained after the integration over the whole transmitted spectral range, are shown in the bottom row of Figure 1. The CF of the SuFI Mg channel reaches right up to the top of the chromosphere, but is not purely chromospheric. It samples both the chromosphere and the photosphere, with the photospheric contribution being 38% of the total in the average quiet sun (the boundary between photosphere and chromosphere is set at 500 km). This fraction is reduced to 24% in the

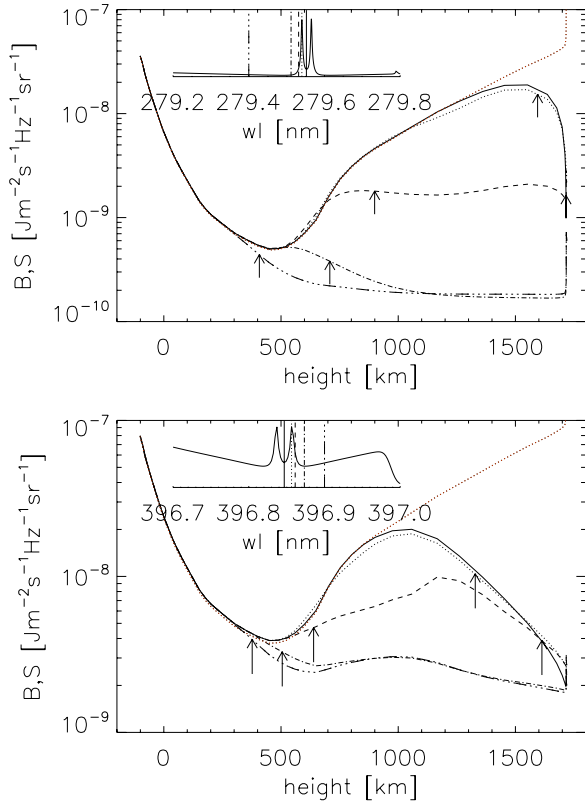


Figure 2. Line-source function at different wavelength positions of Mg II *k* (upper panel) and Ca II H (lower panel) in the FAL-P model atmosphere. Different line styles correspond to the wavelength positions shown in the inserted spectra (solid for the line centers, dotted for the emission peaks, and so on, to the double-dotted-dashed one). Arrows mark the height where $\tau = 1$. The Planck function is displayed by the red dotted curve.

(A color version of this figure is available in the online journal.)

FAL-P model. For Ca, the photospheric contribution is somewhat smaller than for the Ca images from the first SUNRISE flight, which were taken with a 0.18 \AA wide filter (see Figure 2 in Jafarzadeh et al. 2013).

We are aware that the FAL models are only averaged descriptions of the highly structured and dynamic solar atmosphere. However, the CFs in Figure 1 provide some insight into which atmospheric layers are sampled with the SuFI filters and hence by the data analyzed here.

A particularly important point is to check how strongly the line core is coupled to the local temperature because this determines whether the line really samples the thermal structure at the height at which it obtains large contributions, or whether it is already decoupled at that height (it would still sample the velocity and magnetic fields at that height, but for an imager such as SuFI the temperature is the most important atmospheric variable). Figure 2 shows the line-source functions for the wavelength positions marked in the inserted spectra. Similar comparisons have been published by Uitenbroek (1992, 2001) and Milkey & Mihalas (1974). As pointed out in the previous studies, the line-source function calculated in partial redistribution shows a strong frequency dependence. Decoupling from the Planck function takes place at each wavelength at a different height. The behavior is similar for both lines. The line core source function thermalizes higher in the atmosphere because less photons from the line core are being redistributed into the far line wings. The difference is that it occurs lower down for Ca II H than for Mg II *k*. In the

FAL-P atmosphere, Ca II H sees temperatures some $\approx 300 \text{ km}$ lower than the Mg II *k*. More important, the H₂ peaks are strongly decoupled from the temperature corresponding to the source function at $\tau = 1$ (for thermal radiation, i.e., using a Planck function) being $\approx 3600 \text{ K}$ lower than the chromospheric temperature at that height. For Mg II *k*, this temperature difference is only $\approx 800 \text{ K}$.

4. QUIET SUN

In the quiet Sun, both the Mg and the Ca channel images show structures that are reminiscent of reversed granulation. However, there is probably also a considerable contribution as a result of chromospheric (shock) waves (Wedemeyer et al. 2004; Rutten 2007; Rutten et al. 2008). One issue we want to address is whether the Mg and Ca channels display the same structures and whether these structures are due to reversed granulation or shock waves. Finally, we want to address whether the increased fuzziness of the Mg images is solar in origin (because of the differences in formation height and the expansion of magnetic features with height, or the development of the shock waves with height), or has a mixed instrumental (e.g., because of residual image jitter, which is expected to have a larger effect during the long exposure time of the Mg channel) and solar source (e.g., because of the rapid evolution of fine-scale structure during the nearly one-minute integration time of the Mg images).

In Figure 3 we display images at 300 nm, in the Ca, and in the Mg channel in the disk center. These are taken from a sequence in which three images each were recorded rapidly (within 3 s) in the 300 nm and the narrow and broad Ca channels, followed by a single image in the Mg channel. Plotted are the averages of the three 300 nm images recorded just before the Mg image (Figure 3(a)), the three 300 nm images recorded right after the Mg image (Figure 3(b)), the Mg image itself (Figure 3(c)), and averages of the three Ca images before (Figure 3(d)) and after (Figure 3(e)). It is clear from Figures 3(d) with 3(e) that the Ca images change very significantly within the roughly one minute between the two images. Therefore, it is not surprising that each of the Ca images differs equally significantly from the Mg image (Figure 3(c)). This implies that the solar scene changed by a sufficiently large amount during the integration time of the Mg image to make a pixel-by-pixel comparison with an individual Ca image—even if taken immediately before or after the Mg image—impractical. To obtain a Ca image that shows the solar scene as it was roughly at the time of the Mg image, we simply formed the average of the Ca images displayed in Figure 3(d) and 3(e). This average is plotted in Figure 3(f). It shows many of the same features as the Mg image and agrees surprisingly well with it in that the same major features can be recognized in both Figures 3(f) and (c). Even after the temporal averaging, features in the Ca image appear considerably sharper than in Mg. This strongly suggests that the greater width of the features is not, or only to a smaller extent, due to evolution of features during the integration of the Mg image. It also reduces the chance that the increased width is due to image jitter (although that cannot be ruled out completely).

To test this more quantitatively, we plot in Figure 4(a) the averaged Ca II H intensity (Figure 3(f)) versus Mg II *k* intensity. Each dot represents an average of 5×5 pixels (pixel size of $0''.0207$), which still undersamples the resolution of the telescope at these wavelengths. The red line is obtained after calculating means of 0.01 wide bins in Mg normalized brightness. The green line represents a linear fit to the data. A simple averaging of Ca images obtained before and after the Mg image increases the

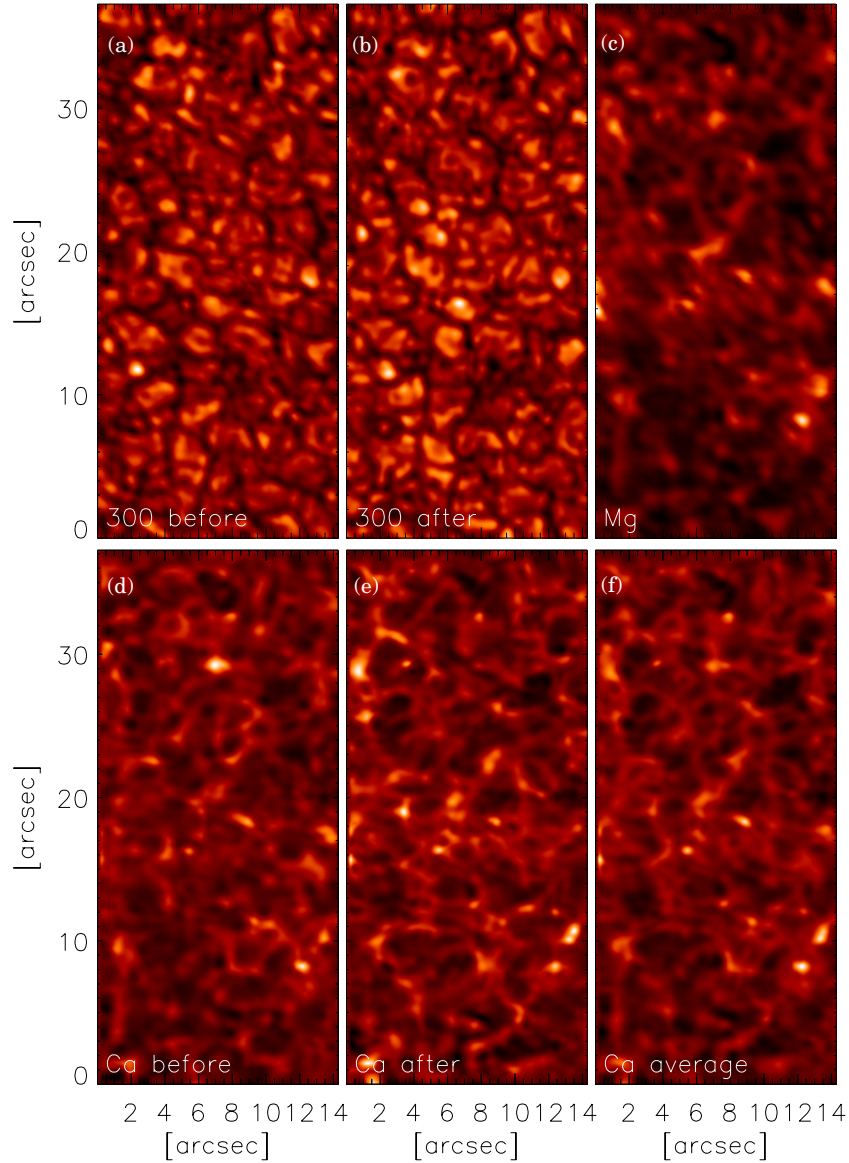


Figure 3. Intensity images in the Mg II *k*, Ca II H, and 300 nm wavelength channels observed by SuFI on June 13 at 12:54 UT ($\mu = 1$). The averaged Ca image is obtained by averaging six images: three that are recorded just before the Mg image and three just after (see the main text for details).

(A color version of this figure is available in the online journal.)

correlation coefficient from 0.81 to 0.87. Much of the scatter is removed in this way. We expect that a comparison between a contemporaneous, equally long integrated Ca and Mg images will result in an even higher correlation. Also, a part of the remaining scatter is due to the low S/N in the Mg image and possibly residual jitter, so that the intrinsic difference between Mg and Ca images is expected to be still somewhat smaller.

The slope of a linear fit to the points in Figure 4(a) is 0.6. This indicates that the intensity contrast in the Mg channel is larger than in the Ca channel by a factor of 1.67. Because there is no clear change in slope at any particular brightness value, this larger range is not just due to the greater brightness of bright points in the Mg channel that had been noted by Riethmüller et al. (2013).

The correlation between Ca and 300 nm is weak and negative, as can be determined from Figure 4(b). Also, the scatter is significantly larger than in Figure 4(a). The correlation between the Mg and 300 nm channels (not plotted) is equally poor and also slightly negative. In fact, it looks very similar to Figure 4(b),

which is not unexpected given the good correlation found in Figure 4(a).

The large scatter and poor correlation in Figure 4(b) implies that the bright features in Ca (and in Mg) do not clearly overlie the dark intergranular lanes in 300 nm (see also the next paragraph and Figure 5). This may relate to the fact that the narrowband Ca filter obtains significant contribution from shock waves in addition to some contribution from reversed granulation. However, this lack of correlation may also be (partly) caused by the fact that the bright lanes of the reversed granulation in Ca are often in the form of two parallel bright lanes that lie on either side of the dark lower-photospheric intergranular lane (Solanki et al. 2010; Riethmüller et al. 2013), so that they are related but often do not properly overlap.

To obtain a quantitative measure of this, the images have been segmented by applying Fourier bandpass filtering and a subsequent thresholding as in Roudier & Muller (1987) and Hirzberger et al. (1997). With this method, we map the location of intergranular lanes that are visible in the 300 nm channel and

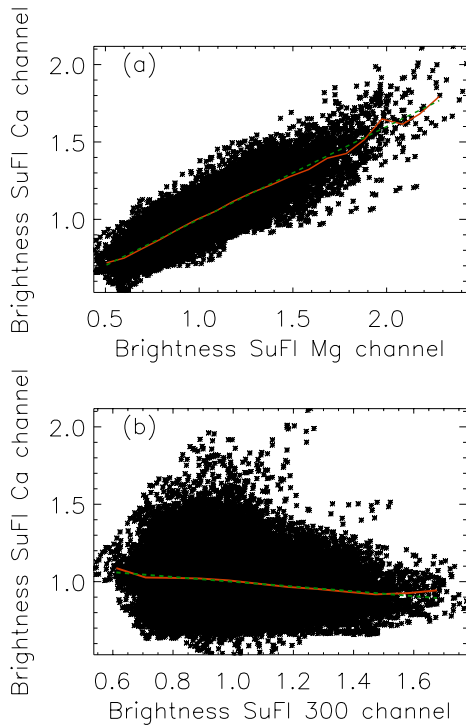


Figure 4. Scatter plots of brightness relations between the Mg II *k*, (time averaged) Ca II H, and 300 nm images shown in Figure 3. The images are normalized to the local mean. Each dot refers to a 5×5 pixel average, and the red solid curves connects bin-averaged values. The green dashed lines mark the linear fit.

(A color version of this figure is available in the online journal.)

compare them with the segmented regions of high brightness in the Mg and Ca channels (with Ca image being the average of the three before Mg images and the three after Mg images). The result is given in Figure 5. The two leftmost frames illustrate the selected regions. A number of less bright lanes, which can be

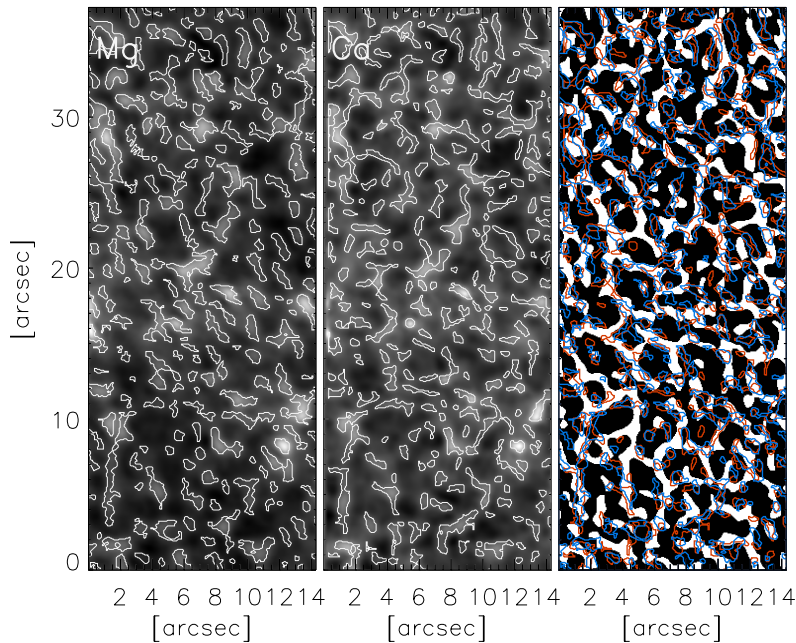


Figure 5. Mg (left) and Ca (middle) images with the bright lanes identified and marked (see the main text). Right panel: intergranular lanes retrieved from the 300 nm channel (white lanes), with contours that mark locations of increased brightness in Mg (blue contours) and Ca (red contours) images, as marked in the left and middle panels.

(A color version of this figure is available in the online journal.)

seen mainly in Ca images, are not included. Some of these, but by far not all, are related to dark lanes in the 300 nm channel and may thus represent reversed granulation. The brightest regions, which are included in the analysis, are located mostly in vertices of granular cells. These are the spots at which hot regions are formed by superposition of neighboring shock fronts (Wedemeyer-Böhm et al. 2009). We also find dark regions inside granule in 300 nm channel coinciding with bright features in both Mg and Ca channels (e.g., $[2'', 14'']$). This matches the exploding granule scenario, where sudden cooling may act as a source of acoustic waves (Rutten et al. 2008; Roth et al. 2010).

In 300 nm images, 32% of the total area of the image is recognized as intergranular lanes. In Mg and Ca images, 24% and 22%, respectively, are identified with bright features. Around 60% of the regions that are bright in Ca are also bright in Mg. This value is lower than the square of the correlation between the two images ($0.87^2 \approx 0.75$). This is probably because the segmentation technique does not identify exactly the same features in the chromospheric images. The significantly smaller, but far from negligible 40%(30%) overlap between 300 nm dark lanes and Mg(Ca) bright lanes suggests that the common (nonmagnetic) bright features in the quiet Sun Ca and Mg images are partly due to reversed granulation and partly due to shock waves.

5. ACTIVE REGION

As discussed by Riethmüller et al. (2013), although the Ca and Mg channel images of an active region at $\mu = 0.41$ reveal many similarities at larger scales, the Ca channel exhibits more fine structures. This can be judged from the two leftmost frames of Figure 6. Riethmüller et al. (2013) also highlighted this difference with the help of a cut across fibrils seen in the Ca and in the Mg channels. Here, we concentrate on a more quantitative comparison than carried out by Riethmüller et al. (2013), starting from the identification of individual fibrils.

Table 1
Characteristics of Fibrils Found in SuFI Channels

Channel	Method	Features	Length		Width		Inclination	
			Mean (Median)	(arcsec)	Mean (Median)	(arcsec)	Mean (Median) [FWHM]	($^{\circ}$)
Mg	Fourier filtering	65	2.4 (1.9)		0.7 (0.5)		37 (34) [25]	
Mg	Unsharp masking	83	2.2 (1.9)		0.6 (0.4)		30 (27) [25]	
Ca	Fourier filtering	111	2.4 (2.1)		0.4 (0.3)		40 (41) [20]	
Ca	Unsharp masking	92	2.5 (2.0)		0.5 (0.4)		43 (44) [20]	

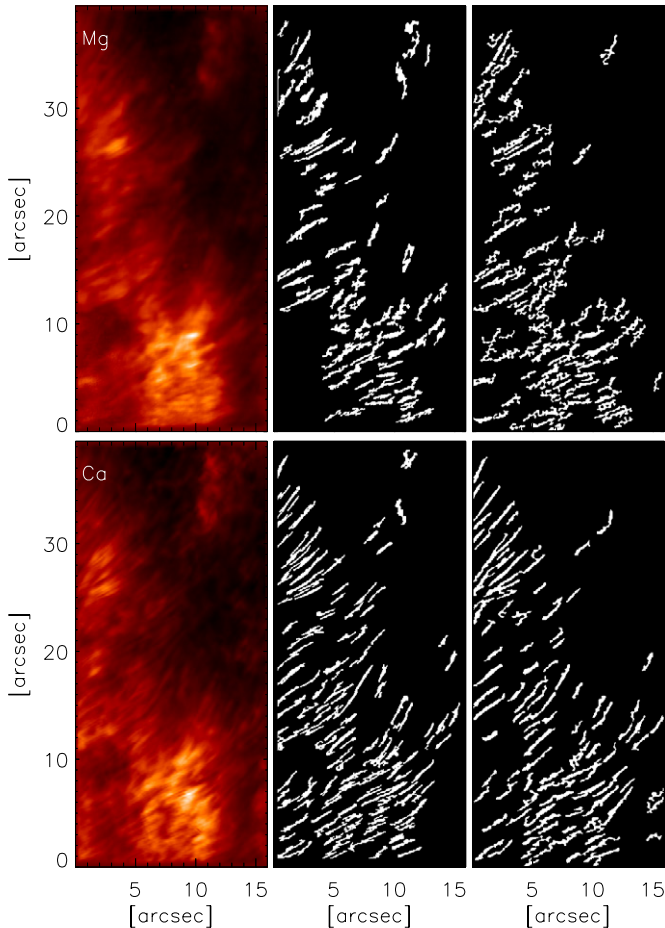


Figure 6. Intensity images in the Mg (top row) and Ca (bottom row) SuFI channels observed on June 16 at 13:13 UT with corresponding masks that outline positions of filaments detected by using two methods: Fourier filtering (middle column) and a set of thresholds combined with unsharp masking (right column).

(A color version of this figure is available in the online journal.)

To avoid comparing arbitrarily identified bright fibrils, we apply two methods to isolate them. Besides Fourier filtering, which was mentioned in the last section, we also follow the procedure described by Pietarila et al. (2009). This method consists of a set of two thresholds combined with unsharp masking with a radius of 15 pixels. Once the preliminary masks are obtained with both methods, we exclude all the preliminary identified regions having less than 200 pixels. Finally, we also exclude all of the detected features with a length smaller than $1\frac{1}{2}$ (50 pixels). These selection criteria are chosen to achieve the best match with visual identification of fibrils in the images. The resulting masks are shown in the middle and right panels of Figure 6.

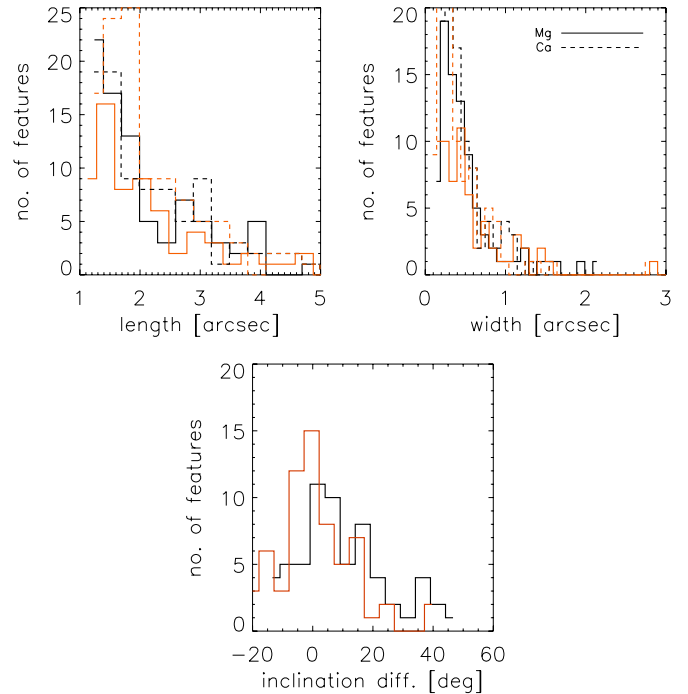


Figure 7. Characteristics of filaments in Mg (solid) and Ca (dashed) SuFI channels detected with two methods: Fourier filtering (red) and a set of thresholds combined with the unsharp masking (black). The rightmost histogram shows the inclination difference between the fibrils found in the two channels. Here, inclination is measured with respect to the vertical axis of the images in Figure 6.

(A color version of this figure is available in the online journal.)

The number of detected features and their characteristics are given in Table 1. The feature characteristics are determined in the following manner. The length is defined as the distance between the two outermost pixels that belong to one feature. A linear fit to all pixels found to belong to one feature is used to determine its orientation in the image, quantified by the inclination relative to the vertical (long) axis of the image. Finally, 10 cuts perpendicular to the fibril's orientation are made, and the final width is obtained by taking the mean value. The distributions of fibril characteristics detected by the two methods are plotted in Figure 7. Instead of the distribution of inclinations of individual channels, the rightmost panel in Figure 7 shows inclination difference between the fibrils found in the two channels.

The two detection methods give qualitatively very similar results. The number of common fibrils found by the two methods in the Mg and Ca images are 58 and 78, respectively, which means that more than 80% of fibrils detected in one method is also detected in the other. The Ca fibrils are on average of the same length or slightly longer than the ones seen in Mg. At the same time, the Mg fibrils are 1.2 or 1.75 times as broad

depending on which of the two methods we use. While the Ca fibrils have a regular shape and rather constant width over their whole length, the widths of the Mg fibrils fluctuate strongly from one location along the fibril to the other. This is most likely (at least in part) due to the higher noise level in Mg images, which makes detection harder and determination of the feature characteristics less precise.

The differences in width of the fibrils in the two SuFI channels could also relate to the longer integration time of the Mg data (50 s versus 500 ms). During that period, the instrumental effects or the evolution of the solar scene could produce such an effect. The former would be the jitter caused by vibrations induced by the continuous movement of the telescope's focus mechanism (more on image stabilization in Berkefeld et al. 2011). To test how large the effect could be, we took a 1 hr time series of SuFI 300 nm images with an exposure time of 100 ms and a cadence of 7 s and calculated the shift between the current image and the image recorded 50 s before (exposure time of Mg). We found values of up to $0''.1$, which is too small to explain the higher smoothness of the Mg images compared to Ca, i.e., the jittering appears to be insufficient to have a major impact on the widths of the filaments. This seems to rule out jitter as the cause. In contrast, as we had seen in the quiet Sun data, chromospheric structures can change significantly over this period of time. Unfortunately, we do not have Ca images both before and after the Mg image displayed in Figure 6. The Ca images recorded by the Swedish Solar Telescope on La Palma at a cadence of 5 s (data were kindly provided by Michiel van Noort) indicate that the filaments evolve more slowly than the shocks and granules seen in the quiet Sun over a 50 s interval. However, not having cospatial and cotemporal Mg images makes it impossible to quantify the effect. So, in summary, either it is an effect of evolving Mg filaments (which we cannot prove that it is too small), or the Mg filaments are intrinsically broader than the Ca filaments (along with a comparatively small effect of the jitter). We cannot say which of the remaining two things has a major effect.

Another possibility to explain the difference in width is that we may simply be seeing different structures in Mg and Ca. This cannot be ruled out, given the rather different sampling of the heights in the plage model atmosphere by these lines (see Figure 1). To test this, we consider the directions of the filaments seen in the two lines. The rightmost panel in Figure 7 shows the difference in inclinations of fibrils detected in the two channels. Only the fibrils that are found to overlap in the two lines, meaning, every Ca fibril that is partially cospatial with at least one Mg fibril is taken into consideration. No limit is set for the size of the overlap. That results in 64 overlapping fibrils for Fourier filtering and 62 for unsharp masking method. The distributions retrieved by the two detection methods both have peaks at 0° . Given that both methods produce similar distributions of orientations for individual channels (see Table 1), we can conclude, with an uncertainty of $\approx 10^\circ$, that most of the fibrils have the same orientation in both channels. This seems to be the case for the regions that contain the brightest fibrils. When we go toward or away from the accompanying sunspot, the fibril brightness decreases and the difference in orientations of Mg and Ca fibrils increases. For such less bright fibrils, the mismatch goes up to 45° . The spread is somewhat larger in case of the unsharp masking method, which seems to produce more irregularly shaped features, which then introduces a larger spread in orientations.

Fibrils detected in SuFI Ca are on average three times wider than the Ca fibrils found in Pietarila et al. (2009). Several

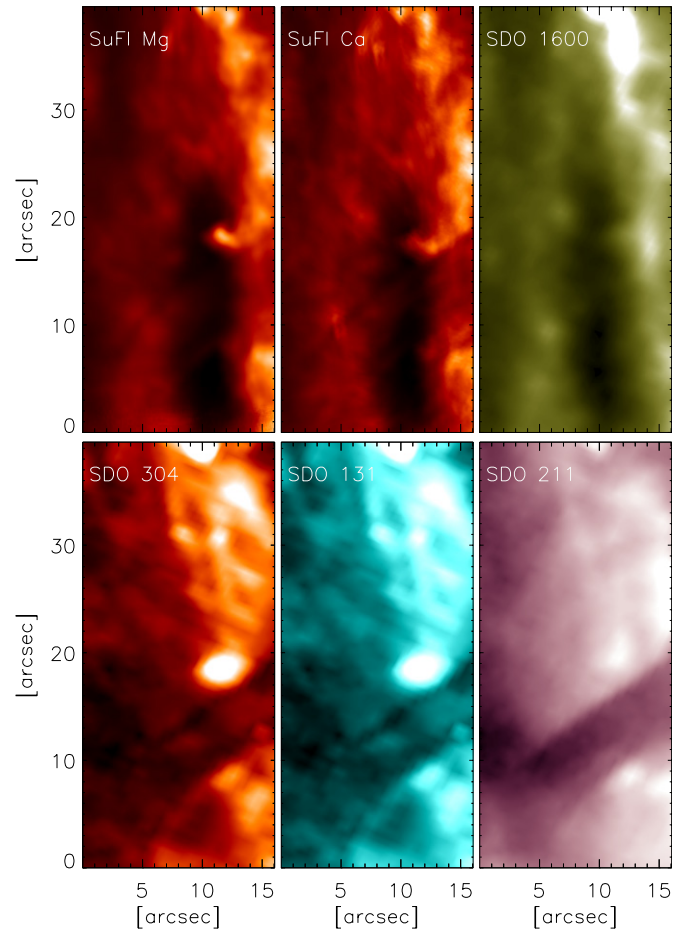


Figure 8. Coarsely aligned SuFI and *SDO* data acquired on June 15 at 19:40 UT. The flaring active region was at the east limb, at $\mu = 0.21$. Images show two interesting features: a filamentary feature at $[7'', 10'']$ and a small surge at $[12'', 20'']$.

(A color version of this figure is available in the online journal.)

reasons could account for this discrepancy. The first would be the difference in the spatial resolution, which is two times higher in the case of the SST observations. Because of that, visual inspection of the detected features shows that unsharp masking with two times larger radius than the one used in the Pietarila et al. (2009) study gives the best result in our case. The discrepancy between the values found by Pietarila et al. (2009) and our result is somewhat smaller when Fourier filtering is used. Also, they looked at the fibrils at the disc center, which might have different properties than the ones close to the limb.

6. A SMALL FLARE

The difference in Mg and Ca filtergrams should be noticeable in extreme scenarios when high velocities and strong increases in temperature arise. Due to its sensitivity to high temperatures near the transition region we expect Mg images to show significantly higher brightness in features with such properties. We find an opportunity to test this in the data taken on June 15 at 19:40 UT, right after a small flare (too small to be registered by the *Geostationary Operational Environmental Satellite*; *GOES*).

A time series of the *Solar Dynamics Observatory* (*SDO*) 304 Å channel shows a coronal loop expanding and erupting at 19:09 UT with subsequent downflow of material that results in a brightening visible in the *SDO* 1600 Å channel. Figure 8 captures the scene some 30 minutes later. The *SDO* data are

aligned and cropped to the SuFI field of view. At this moment in time, the brightening in the 1600 Å channel is still present in the northern part of the active region where the footpoint of the erupted coronal loop is located. Two interesting features are visible in the figure: a filamentary feature at $[7'', 10'']$ and a small surge at $[12'', 20'']$.

This dark (absorption) filamentary structure is long-lasting, as a visual examination of the *SDO* data shows. It lasts at least 1 hr before and after the flare. At 19:40 UT, it is dark in all channels except 1500 Å and 1600 Å, where it is almost (if not completely) invisible. It is also seen in the SuFI filtergrams as a less confined feature than in the *SDO* channels, in the form of dark stripes that are better visible in the Ca channel. The feature seems to be brighter than the underlying sunspot umbra, which suggest the presence of weak emission at chromospheric temperatures.

A small surge appears cotemporally with the brightening in *SDO* 1600 Å images. High-cadence *SDO* data show that it increases brightness in almost all channels simultaneously over 150 s until the instance shown in Figure 8, after which it starts to dim in all the channels. The hot 131 Å and 94 Å channels show a shortest brightening, only few seconds before the dimming phase. This suggests that a temperature of at least 3×10^5 K is reached. The higher resolution SuFI images reveal that the feature seems to have a fine, hook like shape not visible in the *SDO* images. Furthermore, it seems to evolve somewhat differently in the two SuFI channels. While Ca images show the highest intensity always at the bases of the feature, the feature's brightest region seems to move slightly upwards in Mg images. If one takes the region where the apex of the feature appears and compare the brightness in the two SuFI channels, the Mg contrast goes from being less or equal to that in the Ca channel, to being $\approx 40\%$ higher.

7. DISCUSSION AND CONCLUSIONS

The Mg II *k* line is one of the strongest lines formed in the solar chromosphere and is well coupled to the chromospheric temperature structure, as indicated by its strong k_2 peaks and by our computations of its source functions. The SuFI instrument on SUNRISE has provided us with the highest resolution images in Mg II *k* taken so far, with a spatial resolution of around $0''.2$. Here, we present a quantitative comparison of some of the SuFI Mg II *k* images with nearly simultaneously observed images of the Ca II H line core sampled by a 0.11 nm filter.

Before analyzing the data, we computed the CFs of the two lines and multiplied them with the filter profiles. These show that in a standard quiet Sun atmosphere (FAL-C), both channels obtain the largest part of their contribution in the photosphere, although with some differences: for the Ca channel only 36% of the contribution is chromospheric, whereas for the Mg channel this fraction is $\approx 60\%$. In a plage atmosphere (FAL-P), the chromospheric contribution increases significantly to 44% for Ca and $\approx 80\%$ for Mg. Hence, in both cases Mg samples the chromosphere more strongly than Ca, confirming the earlier conclusions by Ayres & Linsky (1976) and Leenaarts et al. (2013b). A comparison of the heights at which the source functions of the two lines depart from the local Planck function also confirms that this happens ≈ 300 – 400 km higher for Mg II k_2 than for Ca II H₂, so that Mg II *k* provides a better picture of the actual chromospheric temperature structure.

We are aware that the atmospheres used for the aforementioned computations are simple standard models that do not

capture the broad range of parameters and stratifications present in the chromosphere and in particular lack the dynamics. However, we expect the aforementioned general conclusions to remain valid, at least in an average sense, also in more complex and dynamic atmospheres, e.g., as result from numerical three-dimensional NLTE-radiation magnetohydrodynamic or hydrodynamic simulations of the solar atmosphere (Leenaarts et al. 2013b).

The images in the two channels look remarkably similar. Both lines display a pattern reminiscent of reversed granulation in the quiet Sun. The Mg images show darker background arising from low-intensity wings (Pereira et al. 2013), i.e., a stronger chromospheric contribution. The broader bright lanes observed in Mg II are only partly explained by the longer integration time of these data (compared with Ca II H) and the rapid evolution of the bright features. An appropriately temporally averaged Ca II image displays a remarkable agreement with a nearly cotemporal Mg II *k* image and a pixel-by-pixel scatter plot reveals a nearly linear dependence (correlation coefficient of 0.87), with the Mg line covering a larger range in brightnesses. This is in agreement with the larger brightness contrasts of the bright points in the quiet Sun detected in Mg than those found in Ca images (see Riethmüller et al. 2013), although the width of the Ca channel obviously also determines the contrasts of the bright points quite strongly.

It is interesting that both Ca and Mg display only a very weak anticorrelation with the 300 nm channel (which shows nearly pure granulation in the quiet Sun). This, together with the comparatively poor spatial overlap of the bright Ca and Mg features with the dark 300 nm features and the more rapid evolution of the chromospheric channels, suggests that the quiet Sun images in the Mg and Ca images are dominated by a combination of shock waves and reversed granulation.

In an active region plage, the Ca and Mg channels both exhibit long, thin fibrils. The fibrils seen in the two lines are qualitatively similar, both having a similar length and point within 10° – 15° in the same direction, although there are locally differences of up to 20° – 40° . However, the Ca filaments are narrower by a factor of 0.6–0.8. We have identified the following possible causes of this difference: different heights and solar fibrils sampled by the two lines, evolution of fibrils during the longer integration of the Mg images, or residual image jitter during the Mg observations. The evidence implies that image jitter and the evolution of solar features during the integration of individual Mg frames can explain only a part of the difference. This suggests that the fuzziness in the Mg images, also in the quiet Sun, is partly intrinsic. We speculate that this is because it is sampling greater heights. In particular, the relatively broad filter is sampling a greater range of heights and, hence, features that do not exactly overlie each other.

During a small flare, the Mg images show 40% higher contrast in a surge, visible also in all *SDO* channels, than Ca II H. The fact that the apex of the feature is significantly brighter in the Mg than in the Ca channel confirms the theoretical study by Pereira et al. (2013). They show that filtergrams taken in the Mg II *k* line through a filter of similar width as SuFI's, will still sample the near-transition region heights, because of the line being wider, with lower-intensity wings. The Ca II H filtergrams will, on the other hand, lack most of the contribution from the larger heights.

The results presented in this paper demonstrate that images taken in the Mg and Ca lines, as sampled by the narrowest currently available interference filters, show remarkable qualitative

and quantitative similarities in the quiet Sun, in an active region plage and during a small flare. In general, Mg does display higher intensity contrasts than Ca, which may have to do with the stronger coupling of the Mg II k_2 peak to the chromospheric temperature than the Ca II H $_2$ peak. Other than this advantage and the slightly better visibility of chromospheric fibrils in Mg (Riethmüller et al. 2013), images in the two spectral lines provide remarkably similar information on the solar chromosphere.

We thank M. van Noort for providing Ca II filtergrams for test purposes. The German contribution to SUNRISE is funded by the Max Planck Foundation, by the *Innovationsfond* of the President of the Max Planck Society (MPG) and by private sponsors. The Spanish contribution has been funded by the Spanish MICINN under project AYA2012-39636-C06. The HAO contribution was partly funded through NASA grant No. NNX13AE95G.

REFERENCES

- Allen, M. S., & McAllister, H. C. 1978, *SoPh*, **60**, 251
- Ayres, T. R., & Linsky, J. L. 1976, *ApJ*, **205**, 874
- Barthol, P., Gandorfer, A., Solanki, S. K., et al. 2011, *SoPh*, **268**, 1
- Beck, C., Rezaei, R., & Puschmann, K. G. 2013, *A&A*, **556**, A127
- Berkefeld, T., Schmidt, W., Soltau, D., et al. 2011, *SoPh*, **268**, 103
- Bonnet, R. M., Lemaire, P., Vial, J. C., et al. 1978, *ApJ*, **221**, 1032
- De Pontieu, B., Title, A. M., Lemen, J., et al. 2014, arXiv:1401.2491
- Fontenla, J., White, O. R., Fox, P. A., Avrett, E. H., & Kurucz, R. L. 1999, *ApJ*, **518**, 480
- Gandorfer, A., Grauf, B., Barthol, P., et al. 2011, *SoPh*, **268**, 35
- Hirzberger, J., Feller, A., Riethmüller, T. L., Gandorfer, A., & Solanki, S. K. 2011, *A&A*, **529**, A132
- Hirzberger, J., Feller, A., Riethmüller, T. L., et al. 2010, *ApJL*, **723**, L154
- Hirzberger, J., Vazquez, M., Bonet, J. A., Hanslmeier, A., & Sobotka, M. 1997, *ApJ*, **480**, 406
- Jafarzadeh, S., Solanki, S. K., Feller, A., et al. 2013, *A&A*, **549**, A116
- Kohl, J. L., & Parkinson, W. H. 1976, *ApJ*, **205**, 599
- Leenaarts, J., Pereira, T. M. D., Carlsson, M., Uitenbroek, H., & De Pontieu, B. 2013a, *ApJ*, **772**, 89
- Leenaarts, J., Pereira, T. M. D., Carlsson, M., Uitenbroek, H., & De Pontieu, B. 2013b, *ApJ*, **772**, 90
- Milkey, R. W., & Mihalas, D. 1974, *ApJ*, **192**, 769
- Morrill, J. S., Dere, K. P., & Korendyke, C. M. 2001, *ApJ*, **557**, 854
- Morrill, J. S., & Korendyke, C. M. 2008, *ApJ*, **687**, 646
- Pereira, T. M. D., Leenaarts, J., De Pontieu, B., Carlsson, M., & Uitenbroek, H. 2013, *ApJ*, **778**, 143
- Pietarila, A., Hirzberger, J., Zakharov, V., & Solanki, S. K. 2009, *A&A*, **502**, 647
- Riethmüller, T. L., Solanki, S. K., Hirzberger, J., et al. 2013, *ApJL*, **776**, L13
- Roth, M., Franz, M., Bello González, N., et al. 2010, *ApJL*, **723**, L175
- Roudier, T., & Muller, R. 1987, *SoPh*, **107**, 11
- Rutten, R. J. 2007, in ASP Conf. Ser. 368, *The Physics of Chromospheric Plasmas*, ed. P. Heinzel, I. Dorotović, & R. J. Rutten (San Francisco, CA: ASP), 27
- Rutten, R. J., van Veelen, B., & Sütterlin, P. 2008, *SoPh*, **251**, 533
- Solanki, S. K., Barthol, P., Danilovic, S., et al. 2010, *ApJL*, **723**, L127
- Staaht, E., & Lemaire, P. 1995, *A&A*, **295**, 517
- Uitenbroek, H. 1992, *Cool Stars, Stellar Systems, and the Sun*, **26**, 564
- Uitenbroek, H. 1997, *SoPh*, **172**, 109
- Uitenbroek, H. 2001, *ApJ*, **557**, 389
- Wedemeyer, S., Freytag, B., Steffen, M., Ludwig, H.-G., & Holweger, H. 2004, *A&A*, **414**, 1121
- Wedemeyer-Böhm, S., Lagg, A., & Nordlund, Å. 2009, *The Origin and Dynamics of Solar Magnetism*, Space Sciences Series of ISSI, Vol. 32 (New York: Springer), 317
- West, E., Cirtain, J., Kobayashi, K., et al. 2011, *Proc. SPIE*, **8160**, 29
- West, E. A., Kobayashi, K., Davis, J. M., & Gary, G. A. 2007, *Proc. SPIE*, **6689**, 12
- Woodgate, B. E., Brandt, J. C., Kalet, M. W., et al. 1980, *SoPh*, **65**, 73